

## Small-scale ultralow-velocity zone structure imaged by *ScP*

Sebastian Rost and Justin Revenaugh

Department of Earth Sciences, Institute of Geophysics and Planetary Physics, Center for the Study of Imaging and Dynamics of the Earth, University of California, Santa Cruz, USA

Received 6 November 2001; revised 29 April 2002; accepted 30 September 2002; published 30 January 2003.

[1] Short-period, teleseismic *ScP* phases from events in the Tonga-Fiji region recorded at the short-period, small-aperture Warramunga Array in Australia are used to study structure at the core-mantle boundary (CMB). We examine the data for evidence of precursors and postcursors to *ScP*. Such additional arrivals are generated by the interaction of *ScP* with structure at the reflection and conversion point at or near the CMB. We show precursors and postcursors to *ScP*, indicating an ultralow-velocity zone (ULVZ) at the CMB in the region between Tonga-Fiji and Australia. One-dimensional forward modeling of the short-period data leads to models of the ULVZ with thickness varying between 5 and 20 km, velocity reductions of 0–10% and 10–30% for *P* velocity and *S* velocity, respectively, and 0–50% density increase. Many events, however, show simple waveforms, consistent with a locally simple CMB. Models for proximal events can vary greatly, indicating very complex, three-dimensional structure with scale lengths of a few tens of kilometers. These results point to complex chemical and physical processes in the lowermost mantle. **INDEX TERMS:** 7207 Seismology: Core and mantle; 8124 Tectonophysics: Earth's interior—composition and state (old 8105); **KEYWORDS:** core-mantle boundary, ultralow-velocity zone, *ScP* waves, seismological array

**Citation:** Rost, S., and J. Revenaugh, Small-scale ultralow-velocity zone structure imaged by *ScP*, *J. Geophys. Res.*, 108(B1), 2056, doi:10.1029/2001JB001627, 2003.

### 1. Introduction

[2] The interface between Earth's core and mantle is perhaps the most significant boundary for the dynamics of the planet. In recent years, several studies have shown that the structural complexities associated with this interface rival those of the crust (see *Garnero* [2000] for a review). Studies have reported a thin zone of greatly reduced *P* wave velocity atop the core-mantle boundary (CMB) in many different regions of the Earth [*Garnero and Helmberger*, 1995, 1998; *Garnero and Jeanloz*, 2000; *Reasoner and Revenaugh*, 2000; *Ni and Helmberger*, 2001], but with a greater percentage of nondetections than detections [*Garnero et al.*, 1998; *Castle and van der Hilst*, 2000; *Persh et al.*, 2001]. These ultralow-velocity zones (ULVZ) might be regions of partial melt [*Williams and Garnero*, 1996; *Vidale and Hedlin*, 1998] and/or zones of chemical contamination of the deep mantle by core material [*Knittle and Jeanloz*, 1989, 1991]. ULVZ are postulated as potential source regions of mantle plumes [*Williams et al.*, 1998] and might possibly control the frequencies of reversals of Earth's magnetic field [*Glatzmeier et al.*, 1999].

[3] ULVZ have been studied with a variety of different seismological methods and phases. Most of the large spatial scale information was obtained using core phases diffracted

along the CMB (*SP<sub>diff</sub>KS*) [e.g., *Garnero and Helmberger*, 1995], core reflected *P* waves (*PcP*) [*Mori and Helmberger*, 1995; *Revenaugh and Meyer*, 1997; *Havens and Revenaugh*, 2001], *PKP* precursors [*Vidale and Hedlin*, 1998] and *S* waves converted to *P* waves at the CMB (*ScP*) [*Garnero and Vidale*, 1999; *Reasoner and Revenaugh*, 2000; *Castle and van der Hilst*, 2000; *Persh et al.*, 2001].

[4] The ULVZ structures found by these studies vary greatly, with thicknesses from ~5 to 50 km, *P* wave velocity ( $v_p$ ) reductions of up to 15% and *S* wave velocity ( $v_s$ ) decreases of up to 45%. The latter velocity and ULVZ density are less well resolved than the other parameters.

[5] *ScP* is exceptionally well suited to study the material properties of ULVZ. The interaction of *ScP* with a simple flat-layer ULVZ structure produces two precursors and one phase arriving after *ScP* (Figure 1). The amplitude of the first precursor, *SdP*, is strongly dependent on density contrast; the amplitude of the last arriving phase, *ScsP*, is primarily sensitive to the shear velocity contrast in the ULVZ [*Garnero and Vidale*, 1999; *Reasoner and Revenaugh*, 2000]. The differential travel time between *SdP* and *ScP* is dependent on the ULVZ thickness and  $v_p$ . Observations of *ScP* with its precursors and "postcursors" offer the possibility of constraining all important material properties in a ULVZ [*Garnero and Vidale*, 1999; *Reasoner and Revenaugh*, 2000], but the additional phases are usually very small in amplitude and are difficult to observe. The Warramunga Array (WRA) data set, however, contains

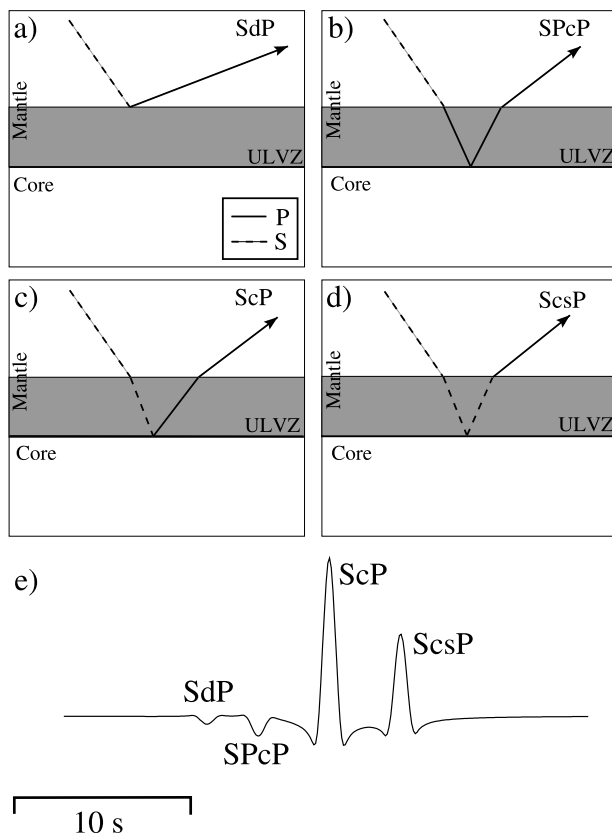


**Figure 1.** Cartoon of the additional phases generated by ULVZ structure at the CMB. (a)  $SdP$  is the reflection at the top of the ULVZ. (b)  $SPcP$  is the conversion of the incident  $S$  wave to a  $P$  wave at the top of the ULVZ. (c) The main phase  $ScP$  is converted from a  $S$  wave to a  $P$  wave at the CMB. (d)  $ScsP$  is reflected off the CMB as a  $S$  wave and is converted to a  $P$  wave at the top of the ULVZ on the way up. (e) Synthetic seismogram showing the additional phases. The modeled ULVZ is 15 km thick with 10% and 30%  $P$  wave and  $S$  wave velocity reductions, respectively, and a 10% density increase. The synthetic seismogram was calculated using Gaussian beam ray tracing [Červený and Pšenčík, 1984; Weber, 1988] with a modified IASP91 model [Kennett and Engdahl, 1991].

some very high  $ScP$  amplitudes and observable precursor and postcursor phases, allowing us to study ULVZ structure over a small region of the CMB in great detail.

[6] In the following, we introduce our data set and modeling techniques, provide example waveforms showing precursors and postcursors and compare these to synthetic waveforms, and discuss the implications for possible structures at the CMB.

## 2. Data

[7] Our data set consists of 270 events originating in the Tonga-Fiji Region (Figure 2). The earthquakes were recorded at the 20-station, short-period, small-aperture Warramunga Array (WRA) located in the Northern Territory, Australia. The earthquakes are deeper than 300 km with magnitudes  $4.3 \leq m_b \leq 6.0$  from the years 1978 to 1986. The source time functions are usually simple, provid-

ing impulsive  $P$  onsets that facilitate modeling. Deep events are selected because shallow events must travel through the highly  $S$  wave attenuating upper mantle reducing  $ScP$  amplitudes. The vertical component instruments of WRA and exclusive use of deep events avoid any possible contamination of  $ScP$  by  $PcS$  due to the larger travel time of  $PcS$  for deep events. The distance range of the data set is  $\sim 40$  to  $45^\circ$ , which is well suited for the detection of  $ScP$ .

[8] We group events into three clusters based on geographical location. Each cluster consists of approximately 90 events. Figure 3 shows the  $ScP$ -to- $P$  amplitude ratios for all events with  $ScP$  visible in individual seismograms of WRA. The amplitudes of the phases were measured in individual raw traces for all stations of WRA and then the mean amplitude ratio for each event was calculated. The amplitude ratios show a large variation with events close to predicted values and up to 2 to 3 times higher amplitudes.

[9] The high amplitudes of  $ScP$  in the south cluster make these events best for the study of ULVZ structure. Very high  $ScP$  amplitudes also have been observed beneath Alaska [Castle and van der Hilst, 2000; Persh et al., 2001].  $ScP$  normally has small amplitudes with  $ScP$ -to- $P$  amplitude ratios  $< 0.1$  [Castle and van der Hilst, 2000]. Unfortunately, only very few source mechanisms for the Tonga/Fiji events used here are known, so that calculating the expected amplitude ratios is difficult. The few known source-mechanisms indicate an increase of the amplitude ratios of the data by 2 to 3 times compared to expected values. Large  $ScP$ -to- $P$  amplitude ratios are, in general, not due to small  $P$  amplitudes. The increase of  $ScP$ -to- $P$  amplitudes can be observed for events with very different source depths, so that slab focusing [Weber, 1990] is unlikely. Different sources for large  $ScP$ -to- $P$  amplitudes have been discussed [Castle and van der Hilst, 2000]: (1) minimal attenuation of  $ScP$  and greater attenuation for  $P$ ; (2) change of the  $ScP$  conversions coefficient at the CMB; and (3) focusing and defocusing of  $ScP$  due to topography at the CMB. CMB topography with scale lengths similar to the  $ScP$  Fresnel zone ( $\sim 50$  km) can increase  $ScP$  amplitude by up to 50% [Castle and van der Hilst, 2000]. Topography on this scale cannot explain the small-scale variation of the  $ScP$  amplitudes we observe for this data set. The  $S$ -to- $P$  conversion coefficient is dependent on the velocity and density contrast across the boundary between the solid mantle and the liquid core. Increasing the  $S$  wave velocity or the  $P$  wave velocity increases the conversion coefficient, whereas decreasing the velocities decreases the coefficient. We do not have information on changes of wave speeds on very small-scale lengths. Most likely some combination of source mechanism and mantle attenuation is the source of the large  $ScP$  amplitudes, as has been proposed for earthquakes in Alaska recorded in the northwestern United States [Castle and van der Hilst, 2000]. A simple dependence on source mechanism has been ruled out as the sole source for the high amplitudes and the differences among the clusters by comparing the known source mechanisms with the amplitude ratios, although source variability undoubtedly is a factor in amplitude variability. The paths of  $ScP$  and the additional phases due to the interaction with ULVZ are very similar so that we expect that the complete  $ScP$  wave field arrives with high energy at the CMB and no differential amplification of parts of the wave field is expected.

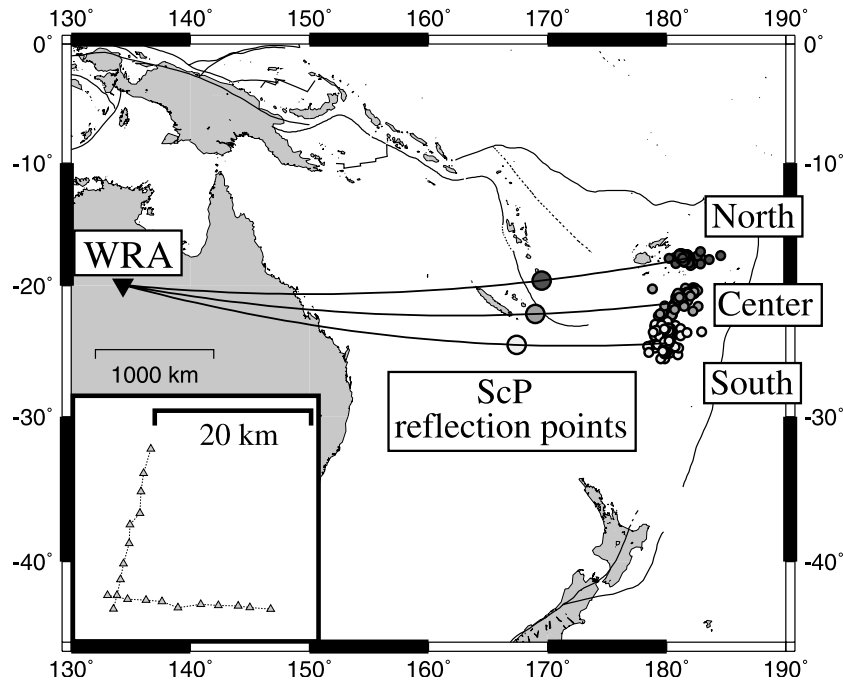


**Figure 2.** Locations of earthquakes (small circles) used in this study. The earthquakes are grouped geographically into three clusters. The large circles indicate the  $ScP$  bounce point region for each cluster. The thin line shows the great circle path from sources to receiver. WRA is indicated by the triangle. The insert shows the L-shaped configuration of the 20 short-period (dominant period,  $T_{\text{dom}} \sim 1$  s) stations at WRA.

[10]  $ScP$  in this data set arrives up to 8 s later than predicted by the IASP91 model of *Kennett and Engdahl* [1991] with most travel times between 2 and 5 s late (we use the event relocations of *Engdahl et al.* [1998] to reduce travel time errors due to source mislocation). A change of the lower mantle  $S$  wave velocity could account for this travel time anomaly. Recent  $S$  wave tomography studies [*Ritsema and van Heijst*, 2000] show a large region of reduced  $v_s$  (up to 1.5%) that is sampled by our data set. The travel time anomalies found here contrast with the high-amplitude  $ScP$  phases documented by *Castle and van der Hilst* [2000], which showed no pronounced travel time anomalies. Both the unusually high  $ScP$  amplitudes and the large travel time delays indicate unusual lower mantle structure in this region of the Earth. The detailed study of the cause of the high  $ScP$  amplitudes and the large  $ScP$  travel time anomaly, however, is beyond the scope of this paper.

[11] The high  $ScP$  amplitudes, especially of events in the south cluster, make it possible to work with individual records and linear stacks from individual events, rather than resorting to stacks of several events or more elaborate array methods like  $N$ th root or phase-weighted stacking [*Reasoner and Revenaugh*, 2000; *Castle and van der Hilst*, 2000]. Figure 4 shows examples of individual (non-stacked) seismograms for the three clusters. Each trace represents one unfiltered station recording of one event. The south cluster (Figure 4a) shows very high  $ScP$  amplitudes. The smallest  $ScP$  amplitudes in the data set are found in the north cluster (Figure 4c). The phase arriving between  $P$  and  $ScP$  in the north cluster is  $PcP$ , which is not as easily observable in the center and south

clusters. We examined all events in the data set for possible indications of ULVZ structure, but because of the high  $ScP$  amplitudes in the south cluster the results are mostly for the southern region.

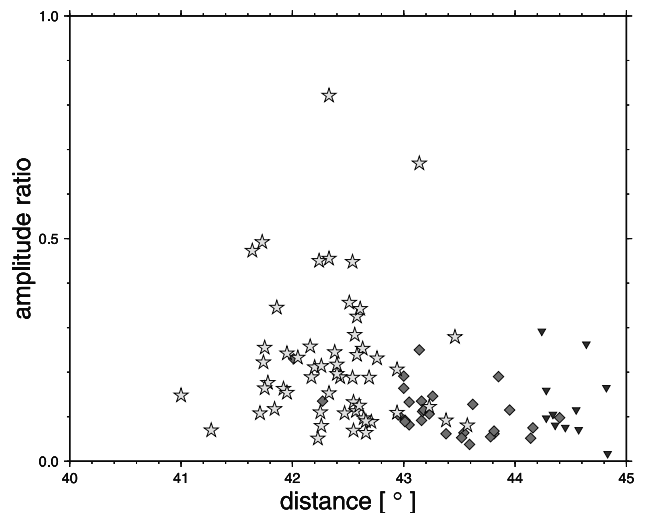


**Figure 3.**  $ScP/P$  amplitude ratios versus distance for the three studied regions. Amplitudes are mean amplitudes for individual events measured on raw traces of the WRA recordings. Events with  $ScP$  above noise level in an individual seismogram of the WRA recordings are shown. Events from the south cluster (stars) typically have  $ScP$  with higher amplitudes than events from the center (diamonds) and the north (triangle).

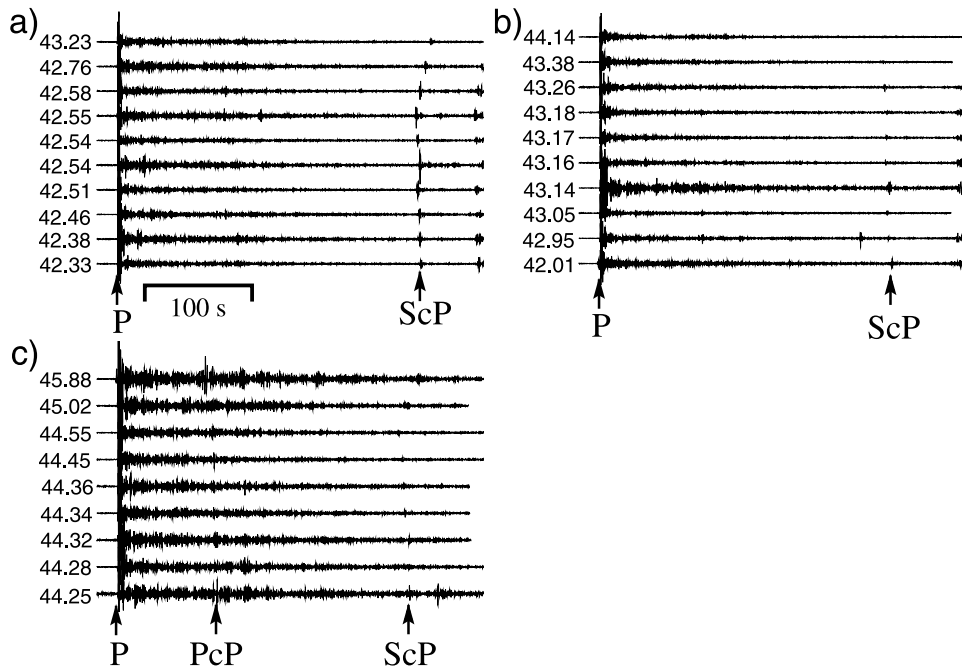


**Figure 4.** Individual station recordings of events from the (a) south cluster, (b) center cluster, and (c) north cluster. Each trace represents the unfiltered recording of one event at one station of WRA. The seismograms are aligned and normalized on the  $P$  onset and sorted by epicentral distance within each cluster. The south cluster shows the highest  $ScP$  amplitudes with amplitudes decaying to the north. The additional onset between  $P$  and  $ScP$  in Figure 4c is  $PcP$ , which shows the highest amplitudes in the north cluster.

[12] Our data processing is minimal. When  $ScP$  amplitude permits, we align the WRA seismograms of individual events on  $ScP$  manually and sum them. For low-amplitude  $ScP$ , we measure the slowness and backazimuth of  $ScP$  with frequency-wave number analysis [Kelly, 1967; Harjes and Henger, 1973] and then use these values for array beam forming.  $P$  wave stacks always are generated by manually aligning  $P$  and summing. Because of the small aperture of the array the waveforms are very consistent across it and little influence of crustal structure beneath the individual stations on the stacked wavelet is observed. To further reduce noise, we filter the stacks with a second-order band pass with corner frequencies of 0.5 Hz and 1.6 Hz. This filter strikes a compromise between reducing noise and maintaining the original waveform.

[13] To infer ULVZ structure, we use forward modeling. We calculate synthetic seismograms for each source-receiver combination using the Gaussian beam method [Červený and Pšenčík, 1984; Weber, 1988], using a line source and IASP91 with velocities and density changed only in the lowermost mantle to fit the  $ScP$  waveform. A line source is used to excite  $S$  waves. Since only a few source mechanisms for the events used are known and because we are concerned only with the relative amplitudes of  $ScP$  and its precursors and postcursors (which have essentially identical slowness), the line source provides a convenient “standard source”. The phases  $P$ ,  $ScP$ ,  $SdP$ ,  $SPcP$  and  $ScsP$  are included in our modeling. Prior to comparing synthetic seismograms with data, we convolve the synthetic seismogram, a spike train due to the simple line source mechanism, with the  $P$  wavelet, which is

representative of the source time function [Vidale and Benz, 1992]. The model space is intensively searched within reasonable limits for thickness, velocity and density variations. Between 25 and 100 different models were tested for each event. The limits of the parameter search depend strongly on the waveform, but thicknesses between 3 to 35 km,  $P$  wave velocity change ( $\Delta v_p$ ) from 0 to  $-15\%$ ,  $\Delta v_s$  from 0 to  $-40\%$ , and  $\Delta \rho$  from 0 to  $50\%$  have been studied.  $P$  and  $ScP$  travel along different paths from source to receiver, have different take-off and arrival angles and different source excitations. Nonetheless, using the  $P$  wavelet as a source for  $ScP$  is feasible as has been shown in different studies [e.g., Vidale and Benz, 1992; Garnero and Vidale, 1999; Castle and van der Hilst, 2000]. Precursors to  $ScP$  are an especially important waveform feature that is specific to the interaction of  $ScP$  with ULVZ and that cannot exist for  $P$ . The coda phase  $ScsP$  is more difficult to interpret since slightly varying structures beneath the array might influence  $P$  and  $ScP$  differently because of the different angles of incidence. For our modeling we use beam traces for  $P$  and  $ScP$ , so that small-scale variations beneath the individual array station can be neglected and the broader-scale structure beneath the array will be sampled by both phases.

[14] A synthetic seismogram prior to convolution is shown in Figure 5a together with the convolution wavelet and the final synthetic seismograms. The effect of the 4 parameters (thickness,  $\Delta v_p$ ,  $\Delta v_s$ ,  $\Delta \rho$ ) is shown in Figures 5a–5d. Only events with simple and impulsive  $P$  waveforms are selected for modeling. Simple  $P$  waveforms are required to reduce interference of the precursors and postcursors with  $ScP$  and

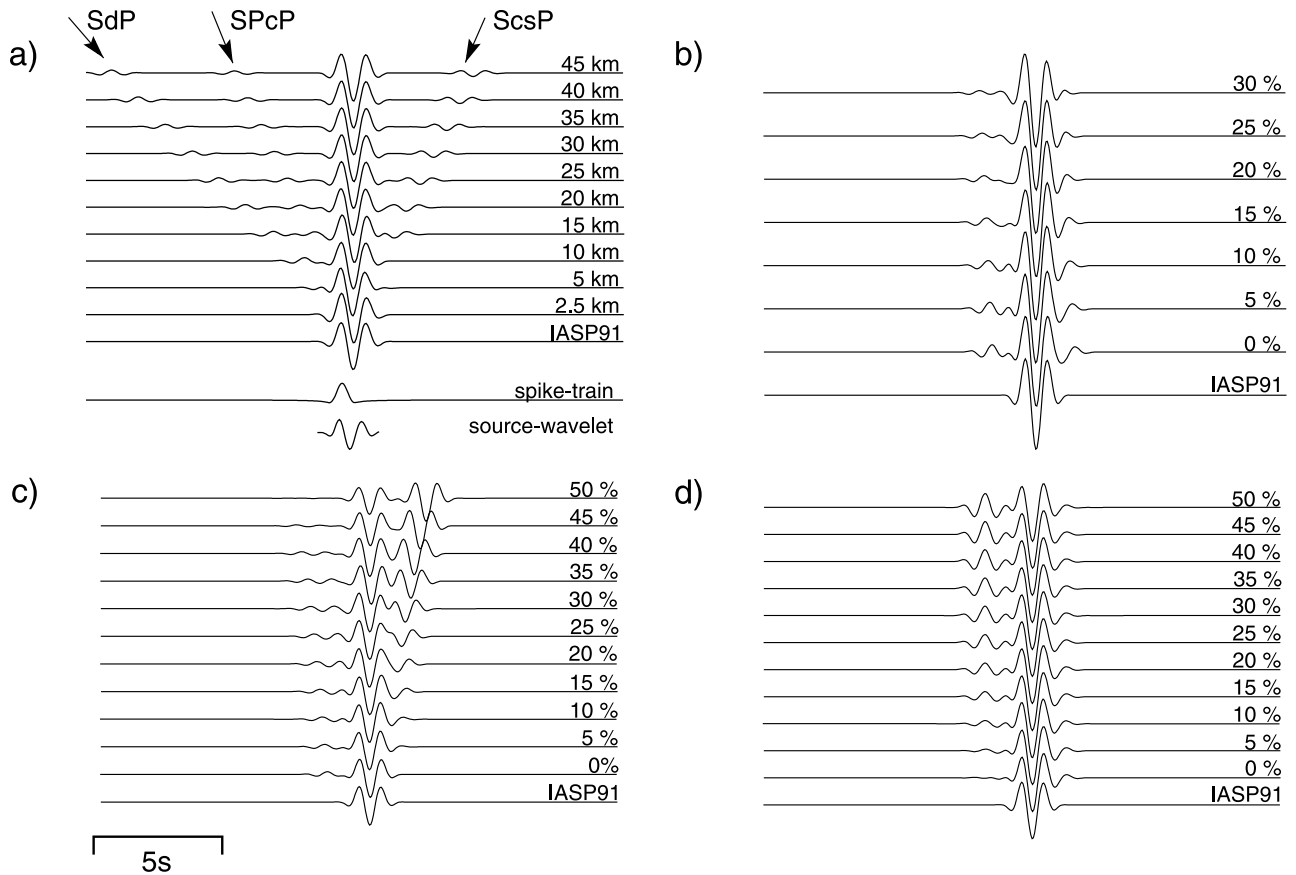


**Figure 5.** Synthetic seismograms showing the influence of the four ULVZ parameters on modeled waveforms [see also *Reasoner and Revenaugh, 2000*]. (a) Thickness of ULVZ is changed, while all other parameters are kept constant. The background model includes a 10%  $v_p$  and  $v_s$  decrease and a 10%  $\rho$  increase. The lowermost trace shows the  $P$  wavelet used for convolution, and the trace above shows the synthetic seismogram for the IASP91 model prior to convolution. A ULVZ around 4 km can be detected by  $ScP$  for the velocity structure assumed here. (b) Variation of  $\Delta v_p$ . The thickness is kept constant at 10 km with  $\Delta v_s = -10\%$  and  $\Delta \rho = 10\%$ . The precursor phases  $SdP$  and  $SPcP$  resolve this parameter. (c) Variation of  $\Delta v_s$ , while the 10-km-thick ULVZ is assumed to show  $\Delta v_p = -10\%$  and  $\Delta \rho = 10\%$ .  $ScsP$  is most sensitive to this parameter. (d) Density variation within the ULVZ, while the velocity shows a decrease of 10% and the ULVZ is 10 km thick. The conversion at the top of the ULVZ ( $SdP$ ) can be used to resolve this parameter.

to obtain nonambiguous ULVZ models. The frequencies of  $P$  and  $ScP$  are slightly different due to differences in  $P$  and  $S$  excitation and a low-pass filtering of  $S$  in the mantle. These differences are small and are included in the modeling by the broad spikes in the spike train.

[15] Our attention is focused on  $ScP$  interaction with ULVZ and CMB structure, thus we do not try to fit absolute  $ScP$  amplitudes or  $ScP/P$  amplitude ratios, nor the observed travel time anomalies of  $ScP$ .

### 3. Observations and Modeling

[16] For all events we compare the  $P$  and  $ScP$  wavelets. For a simple and sharp CMB the waveforms should be equal with the exception of directivity effects, effects of near-source structure and minor differences in crustal reverberations. In the south cluster 53 events show  $ScP$  detectable in individual seismograms. Fewer detections are found

in the central (29 events) and north (11 events) clusters. Not all of these events can be used for modeling because of complicated  $P$  wavelets. Figure 6a shows events in the south cluster with high  $ScP$  amplitudes and simple and matchable  $P$  waveforms arranged according to backazimuth. A precursor to  $ScP$  separated by  $\sim 2$  s can be observed for most of the southernmost events. We interpret this precursor as originating from the interaction of  $ScP$  with ULVZ. Alternatively, it might come from multipathing from topography or from velocity heterogeneities in the lower mantle. But since the differential travel time between the precursor and  $ScP$  is very small, multipathing would only work in a very small region around a central ray, which is unlikely to produce a consistent suite of arrivals that can be modeled by ULVZ structure.

[17] The differential travel time and amplitude of the precursor varies somewhat between the different events. The  $P$  and  $ScP$  linear stacks for all events showing this

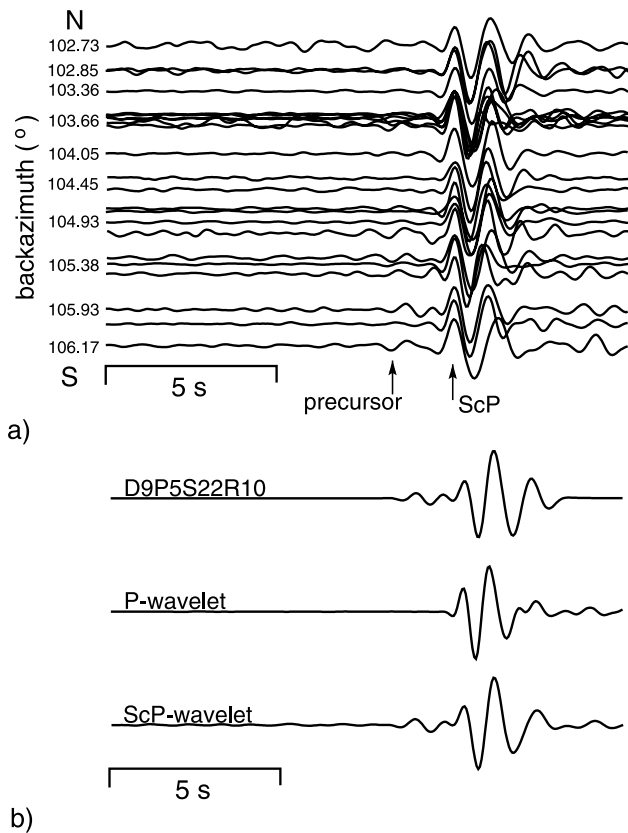


**Figure 6.** (a) Backazimuth-dependent display of high-amplitude *ScP* events with simple *P* waveforms in the southern cluster. Shown are summation traces of *ScP*, which are normalized relative to *ScP* and aligned on the first maximum of *ScP*. The seismograms are aligned on the *ScP* first maximum and are run through a second-order band-pass filter with corner frequencies of 0.5 and 1.6 Hz. The southernmost events, shown on the bottom, show a precursor  $\sim 2$  s before *ScP*, which is not observed farther north. (b) Sum trace of the southernmost 10 events showing a precursor; both summed *ScP* and *P* wavelets are shown. The events were aligned on the first maximum of the wavelet. The *ScP* wavelet is well modeled by a 9-km-thick ULVZ with 5 and 22% *P* and *S* wave velocity reductions, respectively, and a 10% density increase. The labeling convention of the models is *D*, layer thickness (in km) followed by *P*  $v_p$  decrease, *S*  $v_s$  decrease, and *R*  $\rho$  increase (in %).

precursor are shown in Figure 6b. The best fitting model for these averaged events is a 9-km-thick ULVZ with 5% and 22% *P* and *S* wave velocity drops, respectively. The density in this ULVZ is increased by 10% relative to the lowermost mantle. The synthetic seismogram obtained from the model fits the data very well, but we must exercise caution in interpreting this result, which tacitly assumes *ScP* averages structure linearly, i.e., in similar fashion to our waveform averaging. This is not likely to be correct. However, the fact that the derived model is in general consistent with results from other ULVZ probes studying different regions of the CMB is heartening.

[18] As discussed before, the high quality of the data enables us to model individual events. Figure 7a shows

example waveforms of events showing additional phases before and after *ScP*. All events in the south cluster showing evidence of a ULVZ are listed in Table 1 together with the parameters of the one-layer models providing the best fit to the data.

[19] Models derived for individual events display a wide range of parameters. Layer thickness varies from 5 to 20 km. *P* wave velocity shows reductions of 0 to 10% and *S* wave velocity is reduced by 10 to 30%. Density increases vary from 0 to 50%. The spectrum of model structures indicates complex 3-D structure at the CMB varying over very short length scales. Our 1-D models offer insight into this variability, but obviously cannot capture its full essence. In the presence of such structural complexity, 1-D models are necessarily incorrect with biases that we cannot predict. At present, however, this is the best we can do. The high-frequency content of our data prohibits 3-D modeling with current computers and the biases introduced by 2-D modeling are just as unpredictable as those brought on by restricting ourselves to 1-D.

[20] Our interpretation of the models honors these limitations. Details are important only in an ensemble sense and we focus only on broad-scale characteristics of the models. The primary results here are not the individual models, but rather the clear implications of extreme lateral variability in ULVZ form and severity.

[21] Examples of events with simple *ScP* waveforms and no indication of ULVZ structure are shown in Figure 7b. Most of the *ScP* wavelets are very similar to the *P* wavelet. The *ScP* amplitudes of these events are high enough to detect precursors and postcursors, but we find none. A graphical summary of the results for the south cluster is shown in Figure 8. No readily apparent geographical structure of the ULVZ can be identified. Most ULVZ detected are approximately 10 km thick, but the material properties of the ULVZ change drastically on short scale lengths. Some portion of this extreme variability is undoubtedly imposed by our 1-D modeling, but in the absence of short scale length structure our high-frequency 1-D modeling would be correct: our methods may overstate the heterogeneity, but they cannot create it.

[22] No evidence can be found for ULVZ structure in the center and north clusters. Seismograms from these regions are shown in Figure 9. Events in the central cluster sometimes show high *ScP* amplitudes comparable to the south cluster. The *ScP* amplitudes of the north cluster are significantly smaller, making it more difficult to detect ULVZ structure.

#### 4. Discussion

[23] We have demonstrated a number of *ScP* waveforms that are most readily explained by ULVZ at the CMB just west of Tonga-Fiji. Little broad-scale ULVZ structure can be discerned from Figure 8, although some trends are visible. The ULVZ models show thicknesses from 5 to 30 km, with  $\Delta v_p$  from 0 to  $-10\%$ . The *S* wave velocity reductions are in the range from  $-10\%$  to  $-30\%$ , while density increases from 0% to 50% can be found. Some geographical differences in the resolved ULVZ structure can be noted: Events to the south of  $\sim 24.6^\circ\text{S}$  (indicated by the dashed line) have consistent density increases between 10

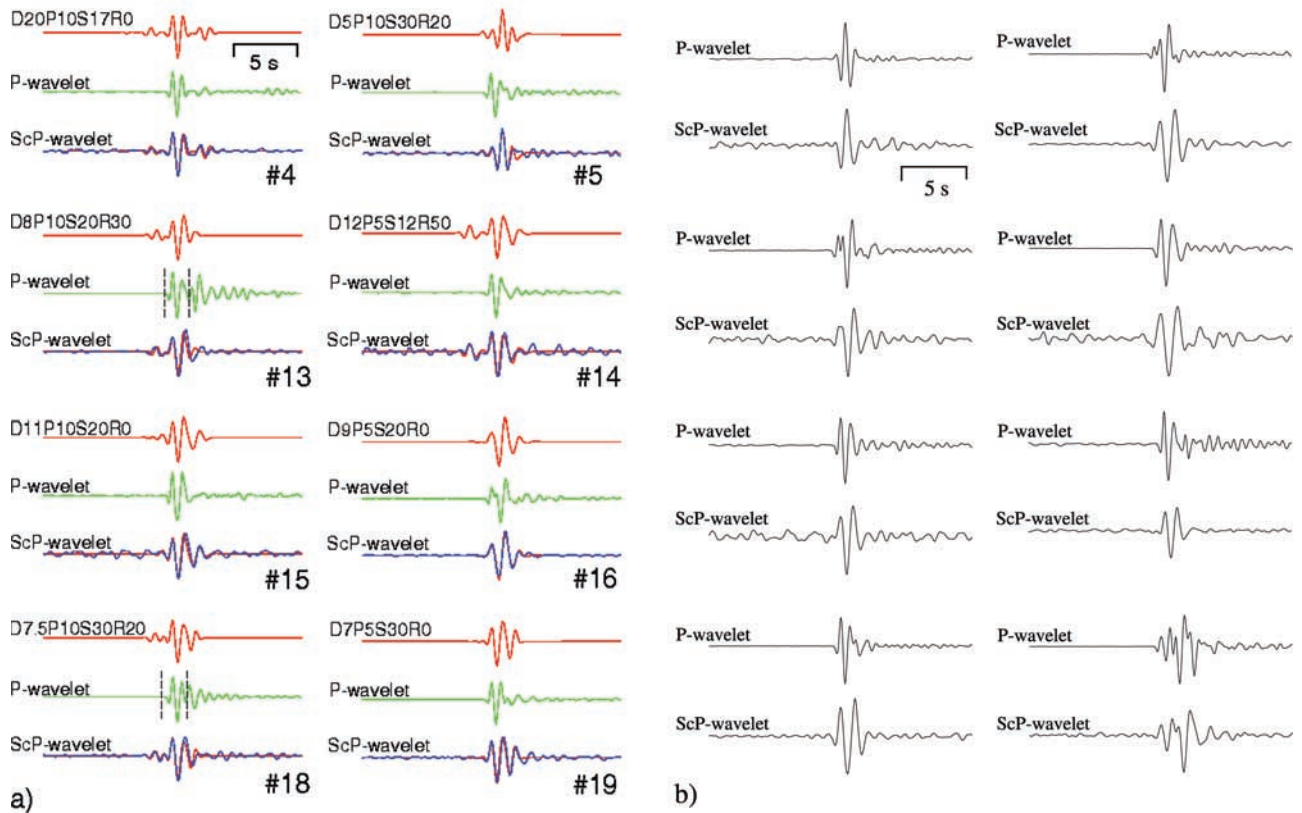


**Figure 7.** (a) Examples of waveforms in the south cluster showing evidence of ULVZ structure. The lowest trace in each panel is the *ScP* waveform (blue line) with the best fitting model (red line) superposed. The model is shown again in the top trace (red line). The middle trace (green line) shows the *P* wave time window for the respective event for comparison. The *P* wavelet has been used as the source wavelet for convolution with synthetic seismograms. For the more complicated *P* waveforms for events 13 and 18 the *P* wavelet used for convolution is marked by the dashed lines. The thickness, density, and velocity changes are given for each model with the convention of Figure 6. (b) Waveforms of non-ULVZ detections from the south cluster. The lower trace in each panel shows the *ScP* waveform; the upper trace is the *P* waveform. The two are very similar.

and 30% in the ULVZ detections, whereas events to the north of  $\sim 24.6^\circ\text{S}$  have no density increase, except for the region where a previous study [Rost and Revenaugh, 2001] observes a thin finite-rigidity zone on the core side of the CMB (CRZ). The waveforms requiring CRZ (marked with stars in Figure 8) do not require very large density increases in addition to the CRZ structure for a better waveform fit, but events in this region detecting ULVZ structure only, require density increases of 40 to 50%, perhaps indicating partial entrainment of core-mantle reactants into the mantle. *S* wave velocity reductions in the northern subset of the south cluster are 10 to 20%, except for the thinnest ULVZ. In the majority of cases the southern subset is characterized by higher  $v_s$  reductions (20 to 30%). Many detections in the northern subset of the south cluster show very small  $v_p$  decreases, but no universal connection between  $\Delta v_p$  and  $\Delta v_s$  in this region can be made.

[24] The density change for the southernmost events is in agreement with the composite model indicated by the waveforms in the south as shown in Figure 6a and points to a large-scale difference between the northern and southern subsets of our ULVZ detections for events in the south cluster. The mean model for the southernmost events shows

a 9-km-thick ULVZ with velocity reductions of 5 and 22%, for *P* waves and *S* waves, respectively, and a density increase of 10%. This mean model exceeds a  $\Delta v_s : \Delta v_p$  ratio of 3:1, indicating partial melt and perhaps some additional velocity decrement due to reaction products [Williams and Garnero, 1996].

[25] The data set shows many nondetections in close proximity to ULVZ (Figure 7b). A ULVZ thinner than  $\sim 3$  km does not noticeably alter the *ScP* waveform, making it impossible to discriminate between  $\leq 3$ -km-thick ULVZ and simple CMB. The short-period waves used here are sensitive to the thickness of the upper boundary of the ULVZ [Reasoner and Revenaugh, 2000], so that nondetections might indicate thicker transition zones at the top of the ULVZ. The closely spaced ULVZ detections and nondetections point to a highly complicated CMB region with significant structure on short scale lengths.

[26] The ULVZ we detect lie several degrees south of a large patch of pronounced ULVZ structure for *P* waves and north of an area with ULVZ nondetection found by  $SP_{\text{diff}}KS$  studies [Garnero et al., 1998]. Vidale and Hedlin [1998] showed that the region ( $8^\circ\text{S}$ ,  $172^\circ\text{E}$ )  $\sim 16^\circ$  north of the area covered by our study area generates unusually large *PKP*

**Table 1.** South Cluster Events Showing *ScP* Precursors and Postcursors<sup>a</sup>

Event	Origin Date	Origin Time, UT	Lat, deg	Long, deg	Depth, km	$m_p$	$\Delta$ deg	$\Theta$ deg	$D$ , km	$\Delta v_p/v_p$ , %	$\Delta v_s/v_s$ , %	$\Delta\rho/\rho$ , %
1	29 Jan. 1979	0543:01.7	-24.722	-179.886	506	5.5	42.31	105.01	8	-5	-30	5
2	3 July 1979	0250:19.8	-23.969	-179.407	466	5.0	42.87	103.98	5	-10	-30	40
3 <sup>b</sup>	12 Nov. 1979	0734:21.1	-24.50	179.70	573	5.0	42.32	104.65	10	-7	-14	0
4	9 Dec. 1979	0109:20.9	-23.823	179.460	530	4.9	41.83	103.67	20	-10	-17	0
5	9 Feb. 1980	1929:16.4	-23.934	179.532	543	5.2	41.89	103.81	5	-10	-30	20
6	15 April 1980	0410:26.9	-24.703	179.912	449	4.9	42.15	104.97	9	-10	-20	20
7	15 Sept. 1980	2121:32.5	-24.243	-179.717	499	5.0	42.54	104.32	8	-10	-20	0
8	1 Jan. 1981	0912:49.1	-23.821	-179.979	514	5.0	42.38	103.71	11	-10	-10	0
9	8 Feb. 1981	0005:22.9	-23.715	-179.947	538	5.3	42.46	103.66	9	-10	-10	5
10	3 May 1981	1249:08.4	-24.934	-179.546	457	5.0	42.68	105.38	10	-8	-25	5
11	17 Aug. 1981	1707:42.9	-25.475	-178.995	387	5.5	43.16	106.17	17	-5	-10	5
12	18 Oct. 1981	1517:16.4	-24.786	179.791	509	4.9	42.04	105.17	9	0	-22	0
13	9 Feb. 1982	1145:30.1	-25.398	-179.938	505	5.2	42.30	105.91	8	-10	-20	30
14	21 Feb. 1982	1418:33.3	-23.913	-179.546	510	5.0	42.65	103.89	12	-5	-12	50
15	6 Sept. 1984	0724:31.0	-23.435	-179.720	540	5.0	42.62	103.12	11	-10	-20	0
16	20 Sept. 1984	1244:26.9	-24.498	-179.766	503	5.2	42.54	104.69	9	-5	-20	0
17	14 March 1985	0626:59.6	-23.680	-179.867	520	4.6	42.49	103.62	5	-5	-30	0
18	13 Oct. 1985	1413:37.3	-25.214	179.996	501	5.1	42.24	105.77	7.5	-10	-30	20
19	24 July 1986	1111:42.6	-23.457	179.963	549	4.9	42.25	103.14	7	-5	-30	0
20 <sup>c</sup>	10 Sept. 1979	0738:41.4	-25.726	179.930	482.5	5.2	42.15	106.56	4	-10	-20	0
21 <sup>c</sup>	20 Nov. 1979	1928:32.4	-24.020	-179.748	530.3	5.0	42.63	103.81	7	-5	-20	0
22 <sup>c</sup>	24 Nov. 1979	0610:40.1	-24.714	178.800	583.3	5.1	41.15	104.97	19	-5	-30	0
23 <sup>c</sup>	6 Jan. 1980	2210:49.6	-23.753	-179.753	504.9	5.0	42.58	103.78	16	-5	-17	0
24 <sup>c</sup>	20 May 1980	0424:47.9	-23.847	-179.722	531.8	5.2	42.59	103.75	33	-5	-10	5
25 <sup>c</sup>	11 Sept. 1980	1030:05.7	-25.795	179.580	507.8	4.9	41.86	106.53	6	-10	-20	0
26 <sup>c</sup>	18 July 1984	0601:54.1	-23.933	-179.516	575.0	4.9	42.77	103.93	4	-10	-10	20
27 <sup>c</sup>	21 Feb. 1985	0656:03.2	-23.904	-179.700	530.6	5.1	42.60	103.94	8	-10	-20	0

<sup>a</sup> $\Delta$  and  $\Theta$  are distance and backazimuth, respectively, of the event to WRA. Source locations are from *Engdahl et al.* [1998]. The best fitting models of ULVZ structure are specified by thickness  $D$ ,  $P$  wave  $\Delta v_p/v_p$ , and  $S$  wave  $\Delta v_s/v_s$  contrasts, and density increase  $\Delta\rho/\rho$ .

<sup>b</sup>USGS source location.

<sup>c</sup>Events showing evidence for CRZ structure [Rost and Revenaugh, 2001].

precursors. They model this with a 60-km-thick layer above the CMB with 13% root-mean-square velocity variation on scale lengths of 10 km which likely requires the presence of partial melt. Other regions of the Pacific studied with *PKP* phases do not show equally large precursors.

[27] Both the *Garnero et al.* [1998] and *Vidale and Hedlin* [1998] studies demonstrate variations of CMB structure on scale lengths of several hundred kilometers. Tomographic images of the CMB in this region are equivocal, but most show a velocity reduction for  $S$  waves and normal to slow  $P$  wave velocity [Grand et al., 1997; Li and Romanowicz, 1996; Liu and Dziewonski, 1998; Masters et al., 1996; Kárason and van der Hilst, 2001; Ritsema and van Heijst, 2000], suggesting warmer than average mantle. Tomography, however, is not able to resolve the lateral and vertical structures on scale lengths of a few tens of kilometers that are manifest in our data.

[28] There are two major competing models for the development of ULVZ: partial melting of the lowermost mantle material and chemical reactions between core and mantle material [Williams and Garnero, 1996]. The reaction between mantle and core material is limited because liquid iron from the core can rise into the mantle along grain boundaries only by capillarity [Poirier and LeMouél, 1992]. The maximum height the liquid can rise is estimated to be only a few tens of meters. Although there are known chemical reactions between core and mantle material [Knittle and Jeanloz, 1989, 1991] these reactions can only take place when the reactants are in contact, restricting the “reaction zone” to the direct vicinity of the CMB unless vigorous small-scale convection stirs mantle material and

reactants [Knittle and Jeanloz, 1991]. This might be happening in the region where CRZs are also detected [Rost and Revenaugh, 2001], as is indicated by the larger density increase required to model the waveforms.

[29] The more likely scenario for the generation of ULVZ, in general, is partial melting of the mantle material due to compositional variability, enhanced heat flux from the core, thermomechanical convection [Hansen and Yuen, 1989], enhanced thermal conductivity [Hofmeister, 1999], or viscous heating [Steinbach and Yuen, 1997, 1999]. Partial melting can account for the 10%  $v_p$  drop in the ULVZ and predicts a  $\Delta v_s:\Delta v_p$  velocity ratio of  $\sim 3:1$  [Williams and Garnero, 1996; Berryman, 2000]. Most best fitting models for the region studied here show a  $\Delta v_p/\Delta v_s$  velocity ratio of 2:1 to 3:1 in good agreement with the partial melt hypothesis (melt content of  $<5-30\%$  depending on the melt texture [Williams and Garnero, 1996]). On the other hand, the density in some structures resolved here, is increased by 10 to 50%, which requires the presence of core material or dense core-mantle reaction products. Nonetheless, infiltration of core material and the resulting iron-silicate reactions cannot account for the  $\Delta v_p$  of  $-10\%$  found here, but only for  $-3$  to  $-4\%$  for a plausible lower mantle chemistries [Williams and Garnero, 1996], unless all fast reaction product are removed from the region.

[30] Experiments demonstrate an enhanced rate of reaction between partially molten mantle silicates and core iron [Ito et al., 1995]. The attendant low viscosity of partially molten mantle results in greater convective vigor and a possible mechanism for producing and distributing a greater volume of core-mantle reaction products. The enormous

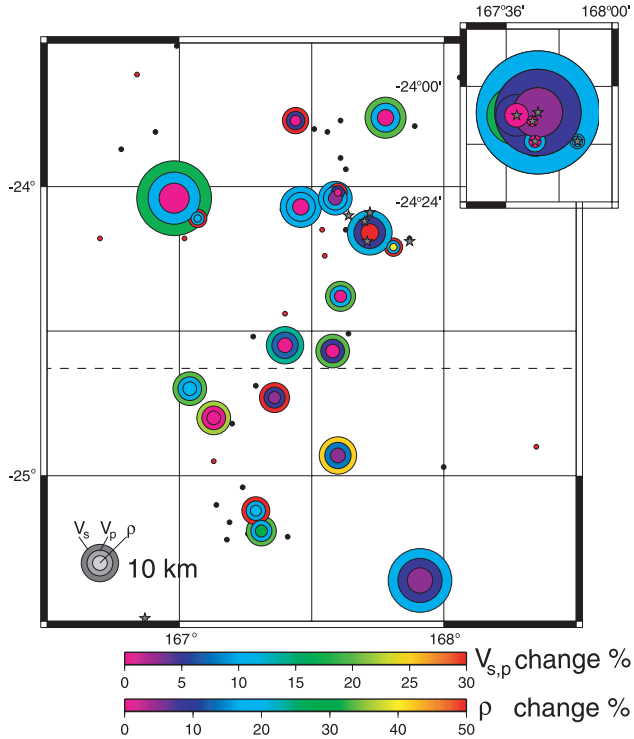


**Figure 8.** Map of all events showing *ScP* structure. The radii of the circles give the thickness of the ULVZ. The symbol size of a 10-km-thick ULVZ is shown in the lower left hand corner in grey scale. The circles are plotted at the bounce point location of *ScP* at the CMB. The two outermost rings of each circle show the *S* and *P* wave velocity reduction in percent relative to IASP91, respectively. The center ring shows the density increase of the best fitting model. Different color scales are used for velocity and density variations. The stars denote the location of inferred core-rigidity zone structure on the core side of the CMB [Rost and Revenaugh, 2001]. Some of these events require ULVZ and CRZ structure to fit the data. The ULVZ structure of the CRZ events are shown in the insert showing the region 167.45°W to 168°W and 23.8°S to 24.4°S. The same scale is used, and the ULVZ models are shown in Table 1. The models include ULVZ and CRZ structure to fit the waveforms. The CRZ structure is chosen as described by Rost and Revenaugh [2001]. Dots mark bounce points where no evidence for ULVZ is found, and the data quality is sufficient to detect postcursor and precursors. Red dots indicate events shown in Figure 7b. The dashed line at 24.6°S separates the northern and southern subsets of the detections, where a difference in density structure is seen.

variability of velocity reductions in the ULVZ found here also may result from vigorous small-scale convection in a thin, low-viscosity zone of partial melt and possible entrained compositional heterogeneities.

[31] Our results show a broad variety of velocity, thickness and density variations within the ULVZ resolved here. The shortcomings of the modeling, namely the restriction to 1-D models, and our lack of understanding about the dynamics of material at core-mantle boundary pressures and temperatures prohibit a final conclusion on the mech-

anism responsible for the apparent structure at this patch of the CMB. We do detect structural differences between the northern and southern parts of the CMB patch studied here. The patch is about 2° by 1° and contains structural differences on scales smaller than the Fresnel zone for *ScP*. We speculate that the density increase and higher  $\Delta v_s$  in the south might indicate an increase in iron atop the CMB, whereas the  $\Delta v_p/\Delta v_s$  velocity ratios in the north might indicate partial melting as the source of the velocity reduction.

## 5. Conclusions

[32] We have examined *ScP* recorded in Australia for events located in the Tonga Fiji subduction complex. We detect additional arrivals that are attributed to the interaction of *ScP* with ultra-low velocity zone structure at the CMB west of Tonga-Fiji. The structures inferred from forward modeling cover a broad spectrum with thicknesses varying from 5 to 20 km,  $v_p$  and  $v_s$  reductions between 0 to 10% and 10 to 30%, respectively and density increases up to 50%. We find many clear nonobservations in close proximity to ULVZ detections. The ULVZ properties in our 1-D modeling change on scale lengths of  $\sim 10$  km indicating very complex 3-D structure in this region of the CMB. Structural differences between the northern and southern part of our study area might be resolved. Events to the north can be modeled without the need for density increases, while southern events require higher  $v_s$  reductions and density

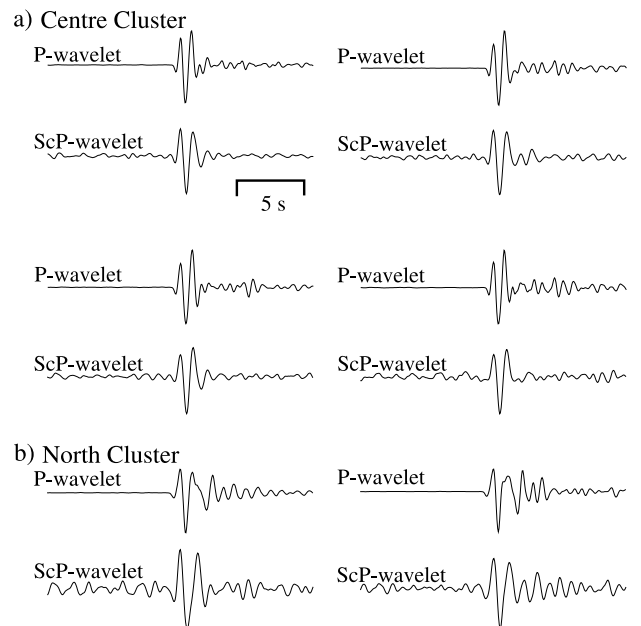


**Figure 9.** Example waveforms for events in the (a) center cluster and (b) north cluster. Events in the center cluster sometimes show high *ScP* amplitudes suited to detection of precursory and postcursor phases. No clear additional phases have been found. The north cluster has much smaller amplitude *ScP* phases with a commensurately smaller probability of identifying ULVZ structure. The events from both clusters show no complicated waveforms. *ScP* appears to interact with a simple CMB.

increases of up to 30%. This might indicate a difference in the mechanism responsible for the ULVZ, with partial melting to the north and entrainment of iron into the mantle in the south. But we have to improve the modeling capabilities for seismic waves and our understanding of core-mantle dynamics, mineral-physics and chemistry to draw final conclusions on these interesting structures.

[33] **Acknowledgments.** We thank G. Jahnke, C. Wicks, and M. Richards for the WRA data set. The figures have been produced using the GMT software [Wessel and Smith, 1995]. Funding for this study was provided by NSF grant EAR-9905733. This is CSIDE (formerly Institute of Tectonics) contribution 455.

## References

- Berryman, J. G., Seismic velocity decrement ratios for regions of partial melt in the lower mantle, *Geophys. Res. Lett.*, *27*, 421–424, 2000.
- Castle, J. C., and R. D. van der Hilst, The core-mantle boundary under the Gulf of Alaska: No ULVZ for shear waves, *Earth Planet. Sci. Lett.*, *176*, 311–321, 2000.
- Červený, V., and I. Pšenčík, Gaussian beams in two-dimensional laterally varying layered structures, *Geophys. J. Int.*, *78*, 65–91, 1984.
- Engdahl, E. R., R. van der Hilst, and R. P. Buland, Global teleseismic earthquake relocation with improved travel times and procedures for depth determination, *Bull. Seismol. Soc. Am.*, *88*, 727–743, 1998.
- Garnero, E. J., Heterogeneity of the lowermost mantle, *Annu. Rev. Earth Planet. Sci.*, *28*, 509–537, 2000.
- Garnero, E. J., and D. V. Helmberger, A very slow basal layer underlying large-scale low-velocity anomalies in the lower mantle beneath the Pacific: Evidence from core phases, *Phys. Earth Planet. Inter.*, *91*, 161–176, 1995.
- Garnero, E. J., and D. V. Helmberger, Further constraints and uncertainties in modeling a mantle basal layer of ultralow velocities, *J. Geophys. Res.*, *103*, 12,495–12,509, 1998.
- Garnero, E. J., and R. Jeanloz, Fuzzy patches on the Earth's core-mantle boundary?, *Geophys. Res. Lett.*, *27*, 2777–2780, 2000.
- Garnero, E. J., and J. E. Vidale, *ScP*: A probe of ultra-low velocity zones at the base of the mantle, *Geophys. Res. Lett.*, *26*, 377–380, 1999.
- Garnero, E. J., J. Revenaugh, Q. Williams, T. Lay, and L. H. Kellogg, Ultra-low velocity zone at the core-mantle boundary, in *The Core-Mantle Boundary Region*, *Geodyn. Ser.*, vol. 28, edited by M. Gurnis et al., pp. 319–334, AGU, Washington, D. C., 1998.
- Glatzmeier, G. A., R. S. Coe, L. Hongre, and P. H. Roberts, The role of the Earth's mantle in controlling the frequency of geomagnetic reversals, *Nature*, *401*, 885–890, 1999.
- Grand, S. P., R. D. van der Hilst, and S. Widiyantoro, Global seismic tomography: A snapshot of convection in the Earth, *GSA Today*, *7*, 1–7, 1997.
- Hansen, U., and D. A. Yuen, Dynamical influences from thermal-chemical instabilities at the core-mantle boundary, *Geophys. Res. Lett.*, *16*, 629–632, 1989.
- Harjes, H.-P., and M. Henger, Array-Seismologie, *Z. Geophys.*, *39*, 865–905, 1973.
- Havens, E., and J. Revenaugh, A broadband seismic study of the lowermost mantle beneath Mexico: Constraints on ultra-low velocity zone elasticity and density, *J. Geophys. Res.*, *106*, 30,809–30,820, 2001.
- Hofmeister, A. M., Mantle values of thermal conductivity and the geotherm from phonon lifetimes, *Science*, *283*, 1699–1706, 1999.
- Ito, E., K. Morooka, O. Ujike, and T. Katsura, Reactions between molten iron and silicate melts at high pressure; implications for the chemical evolution of Earth's core, *J. Geophys. Res.*, *100*, 5901–5910, 1995.
- Káráson, H., and R. D. van der Hilst, Tomographic imaging of the lowermost mantle with differential times of refracted and diffracted core phases (*PKP*, *P<sub>diff</sub>*), *J. Geophys. Res.*, *106*, 6569–6587, 2001.
- Kelly, E. J., Response of seismic arrays to wide-band signals, *Tech. Note 1967-30*, Lincoln Lab., Lexington, Mass., 1967.
- Kennett, B. L. N., and E. R. Engdahl, Traveltimes for global earthquake location and phase identification, *Geophys. J. Int.*, *105*, 429–465, 1991.
- Knittle, E., and R. Jeanloz, Simulating the core-mantle boundary: An experimental study of high-pressure reactions between silicates and liquid iron, *Geophys. Res. Lett.*, *16*, 609–612, 1989.
- Knittle, E., and R. Jeanloz, Earth's core-mantle boundary: Results of experiments at high pressures and temperatures, *Science*, *251*, 1438–1443, 1991.
- Li, X.-D., and B. Romanowicz, Global mantle shear-velocity model developed using non-linear asymptotic coupling theory, *J. Geophys. Res.*, *101*, 22,245–22,272, 1996.
- Liu, X.-F., and A. M. Dziewonski, Global analysis of shear wave velocity anomalies in the lower-most mantle, in *The Core-Mantle Boundary Region*, *Geodyn. Ser.*, vol. 28, edited by M. Gurnis et al., pp. 319–334, AGU, Washington, D. C., 1998.
- Masters, G., S. Johnson, G. Laske, and H. Bolton, A shear-velocity model of the mantle, *Philos. Trans. R. Soc. London, Ser. A*, *354*, 1385–1411, 1996.
- Mori, J., and D. V. Helmberger, Localized boundary layer below the mid-Pacific velocity anomaly identified from a *PcP* precursor, *Geophys. Res. Lett.*, *100*, 20,359–20,365, 1995.
- Ni, S., and D. V. Helmberger, Probing an ultra-low velocity zone at the core mantle boundary with *P* and *S* waves, *Geophys. Res. Lett.*, *28*, 2345–2348, 2001.
- Persh, S. E., J. E. Vidale, and P. S. Earle, Absence of short-period precursors to *PcP* and *ScP* from two regions of the CMB, *Geophys. Res. Lett.*, *28*, 387–390, 2001.
- Poirier, J. P., and J. L. LeMouél, Does infiltration of core material into the lower mantle affect the observed geomagnetic field?, *Phys. Earth Planet. Inter.*, *73*, 29–37, 1992.
- Reasoner, C., and J. Revenaugh, *ScP* constraints on ultralow-velocity zone density and gradient thickness beneath the Pacific, *J. Geophys. Res.*, *105*, 28,173–28,182, 2000.
- Revenaugh, J., and R. Meyer, Seismic evidence of partial melt within a possibly ubiquitous low-velocity layer at the base of the mantle, *Science*, *277*, 670–673, 1997.
- Ritsema, J., and H.-J. van Heijst, Seismic imaging of structural heterogeneity in Earth's mantle: Evidence for large-scale mantle flow, *Sci. Prog.*, *83*, 243–259, 2000.
- Rost, S., and J. Revenaugh, Seismic detection of rigid zones at the top of the core, *Science*, *294*, 1911–1914, 2001.
- Steinbach, V., and D. A. Yuen, Dynamical effects of a temperature- and pressure dependent lower-mantle rheology on the interaction of upwelling with the transition zone, *Phys. Earth Planet. Inter.*, *103*, 85–100, 1997.
- Steinbach, V., and D. A. Yuen, Viscous heating: A potential mechanism for the formation of the ultra low velocity zone, *Earth Planet. Sci. Lett.*, *172*, 213–220, 1999.
- Vidale, J. E., and H. M. Benz, A sharp and flat section of the core-mantle boundary, *Nature*, *359*, 627–629, 1992.
- Vidale, J. E., and M. A. H. Hedlin, Evidence for partial melt at the core-mantle boundary north of Tonga from strong scattering of seismic waves, *Nature*, *391*, 682–685, 1998.
- Weber, M. H., Computation of body-wave seismograms in absorbing 2-D media using the Gaussian beam method: Comparison with exact methods, *Geophys. J. Int.*, *92*, 9–24, 1988.
- Weber, M., Subduction zones—Their influence on traveltimes and amplitudes of *P*-waves, *Geophys. J. Int.*, *101*, 529–544, 1990.
- Wessel, P., and W. H. F. Smith, New version of the Generic Mapping Tools released, *Eos Trans. AGU*, *76*, 329, 1995.
- Williams, Q., and E. J. Garnero, Seismic evidence for partial melt at the base of Earth's mantle, *Science*, *273*, 1528–1530, 1996.
- Williams, Q., J. Revenaugh, and E. J. Garnero, A correlation between ultralow basal velocities in the mantle and hot spots, *Science*, *281*, 546–549, 1998.

J. Revenaugh and S. Rost, Department of Earth Sciences, University of California, Santa Cruz, 1156 High Street, Santa Cruz, CA 95064, USA. (jsr@es.ucsc.edu; srost@es.ucsc.edu)